

Optoelectronic Properties of Two-Dimensional Bromide Perovskites: Influences of Spacer Cations

Dibyajyoti Ghosh,* Amanda J. Neukirch, and Sergei Tretiak*

Cite This: *J. Phys. Chem. Lett.* 2020, 11, 2955–2964

Read Online

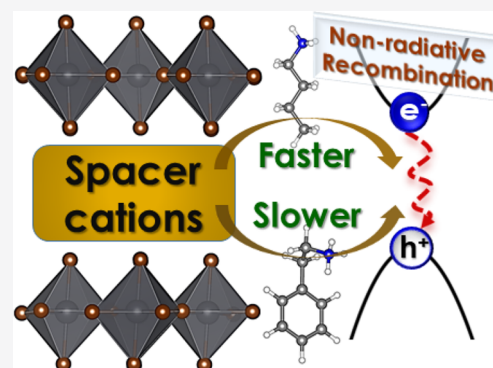
ACCESS |

Metrics & More

Article Recommendations

Supporting Information

ABSTRACT: Two-dimensional (2D) halide perovskites have displayed unique emission properties, making them potential candidates for next-generation light-emitting devices. Here, we combine nonadiabatic molecular dynamics and time-domain density functional theory to investigate the fundamental mechanisms of carrier recombination processes. Considering monolayer bromide perovskites with dissimilar organic spacer molecules, *n*-butylammonium (BA) and phenylethylammonium (PEA) cations, we find a strong correlation between temperature-induced structural fluctuations and nonradiative carrier recombination rates in these materials. The more flexible geometry of (BA)₂PbBr₄ compared to that of (PEA)₂PbBr₄, results in faster electron–hole recombination and shorter carrier lifetime, diminishing the photoluminescence quantum yield for softer 2D perovskites. Reduced structural fluctuations in relatively rigid (PEA)₂PbBr₄ not only indicate of a longer carrier lifetime but also suggest a narrower emission line width, implying a higher purity of the emitted light. Our *ab initio* modeling of excited state properties in 2D perovskites conveys material designing strategies to fine-tune perovskite emissions for solid-state lighting applications.



Two-dimensional (2D) halide perovskites have emerged as one of the most versatile classes of materials for tunable light-emission properties.^{1–6} Depending on the thickness and chemical compositions, these materials exhibit diverse room-temperature emission properties with a wide range of energies as well as spectral widths.^{5,7,8} 2D halide perovskites with extremely narrow emission provide high color purity whereas compounds with broadband white-light emission offer high color rendition.^{6–8,8–11} Several fundamental origins such as exciton localization, structural irregularities, and distortions underpin very different emission in these layered materials.^{12–14} The most commonly explored 2D halide perovskites have a chemical formula of A_nA'_{n-1}B_nX_{3n+1} where A and A' are same or different monovalent organic/inorganic cations, B is the divalent metal ions such as Pb or Sn, and X are the halogens. B_nX_{3n+1} forms the inorganic layer, where BX₆ octahedra have corner-sharing connectivity and A and A' stay either inside the inorganic layer or as the spacer cations between two layers. *n* indicates the number of the metal halide octahedral layers forming the inorganic frame. Optoelectronic properties of these materials are essentially defined by the perovskite component. For example, variation of *n* strongly affects the emission color of 2D halide perovskites.^{15–19} In contrast, organic cations sandwiching the perovskite slabs typically have large gaps and thus do not directly influence the electronic structure.^{13,20–22} However, these molecules ensure structural stabilities, chemostabilities, and photostabilities of

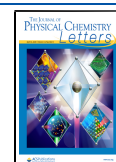
2D halide perovskites are an advantage compared to their 3D counterparts.^{3,23–27}

The highly desired energy-efficient solid-state white light production needs bright and pure blue, green, and red light-emitting materials.^{7,28,29} Among these, materials with a high-quality blue emission are the rarest and consequently form the known bottleneck for advancements in solid-state lighting.^{30–32} The simultaneous necessity for highly efficient luminescence, as well as narrow line width emission, strongly reduces the number of candidate materials for blue emission.³³ In this regard, three-dimensional (3D) chlorine mixed bromide perovskites have been explored widely owing to their wide band gaps, producing sharp emission in the blue region.^{34–36} However, a small exciton binding energy and halide-migration-induced intrinsic phase instabilities result in low photoluminescence quantum yields (PLQY) for these mixed halide perovskites.^{36–39} However, due to substantial quantum confinement, colloidal halide perovskite nanocrystals exhibit color pure and strong blue luminescence.^{40–42} Nonetheless, strong emission intermittency, i.e., PL blinking and poor

Received: February 23, 2020

Accepted: March 25, 2020

Published: March 25, 2020



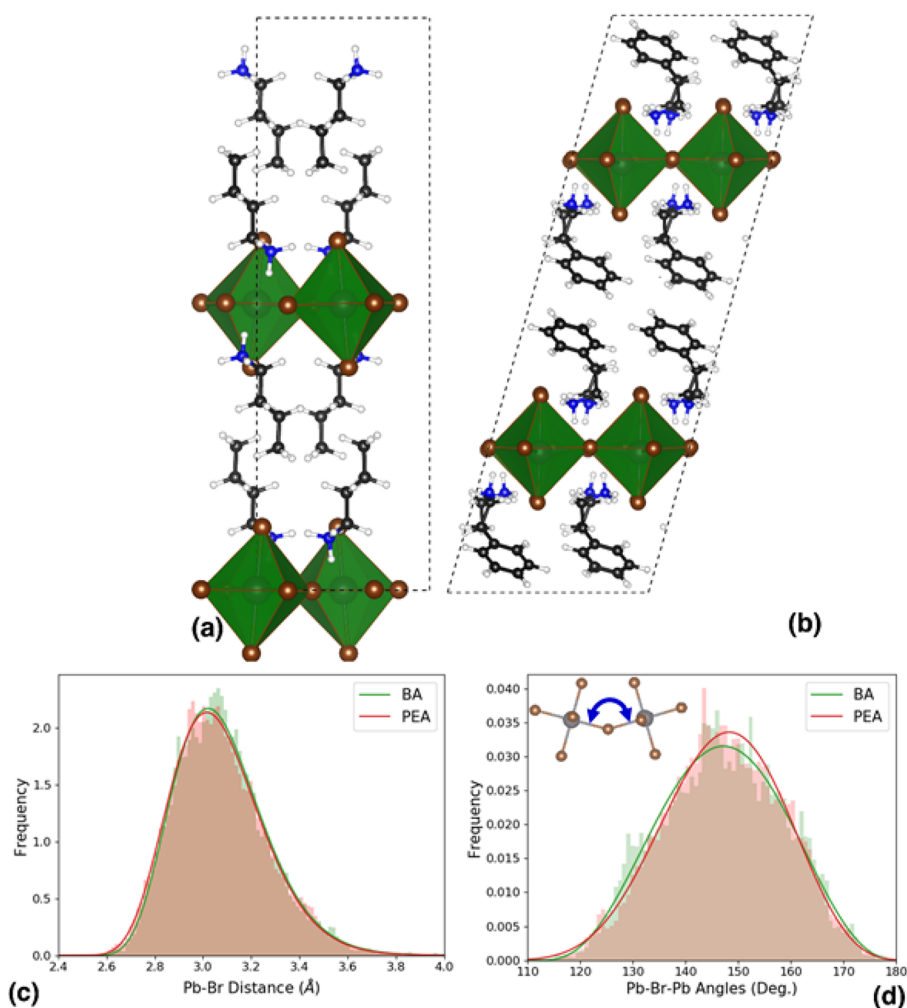


Figure 1. Optimized structures and their fluctuations at room temperature. Optimized structures of $1 \times 1 \times 1$ cells for (a) $(\text{BA})_2\text{PbBr}_4$ and (b) $(\text{PEA})_2\text{PbBr}_4$. Colors: hydrogen (white), carbon (black), nitrogen (blue), bromine (brown), lead (gray). The histograms for (c) Pb–Br bond lengths and (d) in-plane Pb–Br–Pb bond angles as shown in the inset evaluated over AIMD simulation trajectories of these 2D perovskites. Broader distribution of metal bromide angles for BA-based perovskites is evident in (d). Solid lines in (c) and (d) are fitted by the β -function to the distributions.

performance in light-emitting diode (LED) architectures, poses serious challenges to fabricate nanocrystal-based blue emitters.^{43,44} Recently, quantum-well structures of 2D halide perovskites have been actively explored to fine-tune their blue emission properties.^{3,6,11,45–49} Spatial excitonic localization and consequent fast radiative electron–hole recombination in wide band gap 2D perovskites make these materials suitable for blue emission.^{21,50} Despite these promising findings, the dominant presence of nonradiative recombination has been identified as the fundamental reason for the low PLQY of 2D perovskite-based blue LEDs.^{5,51} The resonance Raman spectroscopy and deformation-potential-based analysis by Gong et al. demonstrated that fast nonradiative recombinations originate from the strong electron–phonon interactions in the flexible 2D perovskites.¹¹ The study further proposed that room temperature emission properties of these perovskites can be largely tuned by using different spacer cations. It is well-known that the spacer cations substantially affect the crystal structure of the 2D perovskites and distort the inorganic layers to a different extent.^{2,52,53} The static distortion in inorganic layers further influence the optical band gap and exciton binding energies of these materials.^{51,54} More recently, it has

been found that structural dynamics and particularly its effect on carrier transport also considerably affect the optoelectronic properties of 2D perovskites.^{11,27,55,56} Despite a number of experimental observations,^{6,11,45–47} we still have little understanding of an in-depth atomistic structure–property relationships controlling excited-state dynamics in these materials at room temperature.

Recently, we have investigated the quantum confinement effects in low-dimensional halide perovskites and subtle effects of structural fluctuations on the optoelectronic properties of their 3D counterpart.^{12,21,57–59} In the present contribution, we use *ab initio* time-domain simulations to explore the charge carrier relaxation and recombination processes in monolayered lead bromide perovskites, $(\text{A})_2\text{PbBr}_4$, where A is the spacer cations. Considering alkyl-chain-based *n*-butylammonium (BA) and benzene-ring-based phenylethylammonium (PEA) as the spacer cations, we find these molecules significantly influence the structural dynamics of the inorganic PbBr_4 layer (Figure 1). This gives rise to strong electron–phonon interactions and quantum decoherence, resulting in very different nonradiative carrier recombination rates that control the emission properties of these materials at room temperature.

A detailed understanding of the structural dynamics dependent light-emitting properties further helps to guide design principles for achieving high-quality 2D perovskite-based emitters.

Structural Properties. Analysis of optimized internal geometries (see Computational Methods for simulation details) of $(\text{PEA})_2\text{PbBr}_4$ and $(\text{BA})_2\text{PbBr}_4$ as shown in Figure 1a,b reveal that noncovalent interactions between organic spacer cations and the PbBr_4 layer affect their static ground-state structures. In $(\text{PEA})_2\text{PbBr}_4$, apical Pb–Br bonds of the PbBr_6 octahedron have different lengths, one elongates (3.26 Å) and other contracts (2.91 Å), whereas all equatorial lead–halide bond distances are similar (3.05 Å) (Figure S1). However, all apical and equatorial Pb–Br bonds for $(\text{BA})_2\text{PbBr}_4$ are of almost same lengths (~ 3.02 Å) (Figure S1). These bond distances are in a good agreement with the experimental structures, resolved by single-crystal X-ray diffraction.¹¹ As we are mostly interested in room temperature structures of these 2D bromide perovskites and their optoelectronic properties, static geometries are not explored any further.

Ab initio molecular dynamics (AIMD) simulations at 300 K show that the Pb–Br bond lengths in both perovskites increase with respect to optimal bond lengths due to the thermal expansion of the lattices. The canonical average of Pb–Br bond lengths show that these are slightly shorter in $(\text{PEA})_2\text{PbBr}_4$ (3.07 Å) compared to those in $(\text{BA})_2\text{PbBr}_4$ (3.09 Å). Additionally, for PEA-based perovskite, thermal fluctuations largely suppress the distinct difference in apical Pb–Br bond lengths that we find in 0 K optimized structure (see Figure S2). Plotted histograms of the Pb–Br bond lengths in Figure 1c exhibit non-Gaussian distribution for both structures, demonstrating intrinsic lattice anharmonicity of these 2D perovskites. A similar anharmonic nature in 3D perovskites has been reported in the context of charge carrier dynamics.^{60,61} Detailed discussion on the effect of thermal fluctuations of the Pb–Br bond lengths has been included in the Supporting Information (section S1). Moreover, we calculate the Pb–Br–Pb angle distribution in the *ab*-plane as a measure of in-plane PbBr_6 octahedra tilting in these systems (see Figure 1d). Canonically averaged Pb–Br–Pb angles indicate that PbBr_6 octahedra are tilted by $\approx 33^\circ$ for both the perovskites at room temperature. However, plotted histograms indicate a wider angle distribution for $(\text{BA})_2\text{PbBr}_4$, signifying more fluctuating Pb–Br–Pb angles in this perovskite with respect to that in $(\text{PEA})_2\text{PbBr}_4$. The standard deviation of the Pb–Br–Pb angle values for $(\text{PEA})_2\text{PbBr}_4$ and $(\text{BA})_2\text{PbBr}_4$ are 11.5° and 11.3° , respectively. To have a quantitative description of thermal fluctuations, we further calculate the root mean square fluctuations (RMSF) for Pb and Br atoms in both perovskites. As shown in Figure 2, Pb and Br exhibit higher RMSF in $(\text{BA})_2\text{PbBr}_4$ compared to results for $(\text{PEA})_2\text{PbBr}_4$, clearly demonstrating more flexible inorganic layers for long-alkyl-chain-based 2D perovskites. Moreover, the carbon and nitrogen atoms of the BA cations show higher RMSF compared to the PEA cations. The CH- π stacking among the PEA cations restricts their thermal motions between two PbBr_4 layers, whereas the absence of any such interactions among the alkyl BA cations results in more flexibility in these chain-like molecules. More spacer cation fluctuations, in turn, introduce more structural dynamics in PbBr_4 layers for these materials. Thus, our analyses demonstrate that packing of spacer cations into a inorganic

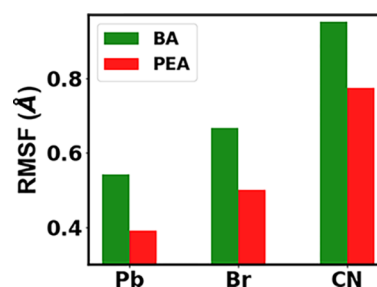


Figure 2. Effect of spacer cations on the lattice dynamics of 2D perovskites. The root mean square fluctuations for Br, Pb, and organic cations (considered only C and N atoms) at 300 K exhibit more dynamical structural behavior of $(\text{BA})_2\text{PbBr}_4$ compared to $(\text{PEA})_2\text{PbBr}_4$. The long-chain BA cations allow for more thermal fluctuations in the inorganic layers.

lattice determines the extent of room temperature structural motions in these 2D perovskites.

Electronic Properties. We further investigate the electronic properties of $(\text{BA})_2\text{PbBr}_4$ and $(\text{PEA})_2\text{PbBr}_4$. Starting with the geometries optimized with the PBE functional (see Computational Methods), spin–orbit coupling (SOC) corrected HSE06 functional-based simulations provide the band gap values for $(\text{BA})_2\text{PbBr}_4$ and $(\text{PEA})_2\text{PbBr}_4$ as 3.13 and 3.14 eV, respectively. The band gap values are in a good quantitative agreement with the recent experimental observations.¹¹ The projected density of states (pDOS) (Figure 3a,b) and charge densities at the band edges (Figure 3c–f) indicate that the antibonding overlap of Pb 6s and Br 4p* orbitals forms the

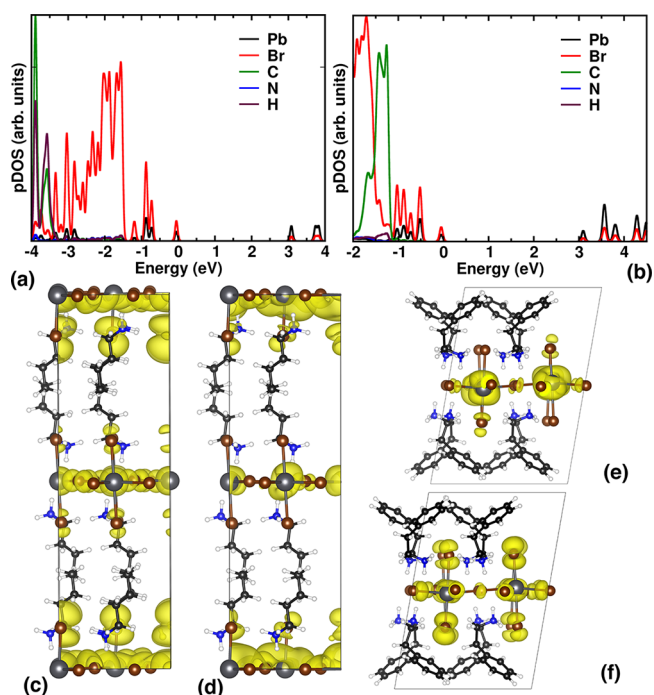


Figure 3. Electronic structure of 2D bromide perovskites. Partial density of states for (a) $(\text{BA})_2\text{PbBr}_4$ and (b) $(\text{PEA})_2\text{PbBr}_4$. Prominent cationic states appear near VBM for PEA-based perovskites. The electronic charge densities of (c) VBM and (d) CBM for BA-based perovskites. (e) VBM and (f) CBM charge densities of $(\text{PEA})_2\text{PbBr}_4$. All the band edge densities are located in the inorganic layer. Presented electronic structures are calculated using the HSE06 functional including SOC corrections.

valence band maximum (VBM) whereas the conduction band minimum (CBM) originates mostly from nonbonding Pb 6p orbitals. Parts a and b of Figure 3 illustrate that the molecular orbital energy states of organic spacers remain a few electronvolts above and below from the CBM and VBM, respectively. Thus, the spacer cations do not directly participate in the electronic structure near the band edges in these 2D bromide perovskites. Note that, compared to the BA, the PEA molecular states in $(A)_2\text{PbBr}_4$ remain close to VBM (~ 1.27 eV), suggesting their possible influences to the hot-hole relaxation processes in the material (Figure 3b).⁶² The similar band gap and band edge electronic properties of these two 2D perovskites at 0 K strongly suggest that the static geometries are not sufficient for understanding their very different excited-state dynamics and room temperature PLQY.

This necessitates investigation of structural dynamics on the electronic properties of 2D perovskites at room temperature. Plotted histograms in Figure 4 show that the band gap of

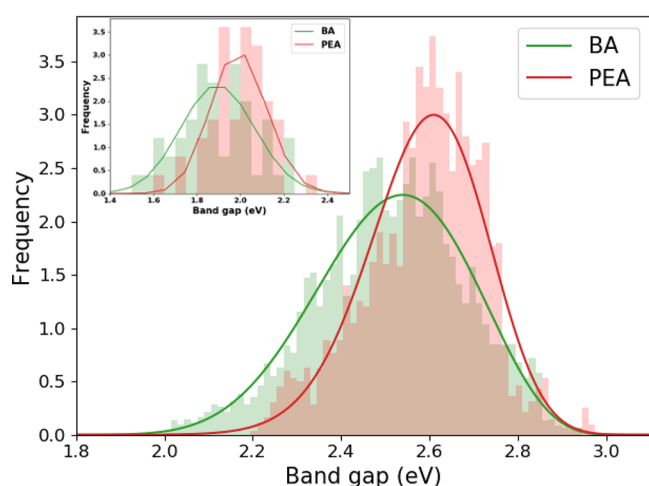


Figure 4. Fluctuations in the electronic structure of 2D bromide perovskites at room temperature. The histogram of the PBE band gaps along the AIMD trajectories for $(\text{BA})_2\text{PbBr}_4$ and $(\text{PEA})_2\text{PbBr}_4$. The band gaps have a broader distribution in BA-based bromide perovskite. The upper left corner shows the histogram of band gaps for a selected number of snapshots calculated including the SOC correction. The trend of band gap distributions remains unchanged with or without SOC correction. Solid lines are fitted by a β -function to the distributions.

$(\text{PEA})_2\text{PbBr}_4$ has a narrower distribution compared to that of $(\text{BA})_2\text{PbBr}_4$. The standard deviation of band gap values for PEA- and BA-based perovskites are 0.12 and 0.17 eV, respectively. This is directly related to pronounced structural fluctuations observed in the inorganic framework of $(\text{BA})_2\text{PbBr}_4$. As both the VBM and CBM are delocalized only over the PbBr_4 layer (see Figure 3c–f), a more flexible inorganic frame in $(\text{BA})_2\text{PbBr}_4$ results in the stonger fluctuations of the band edge energy positions and produces a wider spread of band gap values.

As spin–orbit coupling significantly influences the band edge electronic structure of these 2D perovskites, we further calculate the band gap fluctuations along the simulated trajectories incorporating the SOC corrections.^{22,63–65} To reduce the high computational cost for SOC included simulations, we chose random 50 snapshots that are equally spaced in simulation time. As plotted in the inset of Figure 4, even though the band gaps are underestimated by ≈ 1 eV for

both the systems, $(\text{BA})_2\text{PbBr}_4$ exhibits more dispersion in band gap values compared to that in $(\text{PEA})_2\text{PbBr}_4$. The severe band gap reduction with the inclusion of SOC originates from the downward shift of Pb 6p-orbital dominated CBM as well as the absence of electronic many-body interactions in these calculations.^{58,66} Though using the HSE06 functional along with SOC provides band gaps comparable to the experimental reports, such calculations for many snapshots are extremely computationally demanding and are not presently performed. Nonetheless, the trend in the average band gap and their fluctuations for $(\text{BA})_2\text{PbBr}_4$ and $(\text{PEA})_2\text{PbBr}_4$ remain unaltered with or without incorporating SOC in the calculations. This further suggests the dominant role of structural dynamics determining the band-edge fluctuations in these 2D perovskites.

Charge Carrier Recombination. Structural fluctuations in soft halide perovskite lattices significantly affect their excited-state dynamics at ambient conditions.^{67–71} Extensive experimental and computational investigations have identified strong dependence between charge carrier lifetime and structural rigidity in a variety of inorganic and hybrid halide perovskites.^{55,72–74} Here, we further perform nonadiabatic molecular dynamics (NAMD) to explore the nonradiative carrier recombination dynamics near the band edges of monolayer 2D bromide perovskites. We include the influence of all the energy states residing near to the band edges for the excited-state dynamics simulations (see Computational Methods for details). Figure 5a displays time evolved population of charge recombined state evidencing much faster nonradiative electron–hole recombination for $(\text{BA})_2\text{PbBr}_4$ compared to that for $(\text{PEA})_2\text{PbBr}_4$. Slow electron–hole recombination in halide perovskites demands computing carrier dynamics for the time scale on the order of tens of nanoseconds which is computationally challenging.⁷³ To overcome such issues, we apply the short-time linear approximation of the exponential increase and compute the recombination time of these 2D bromide perovskites (see section S2 in the Supporting Information for details).^{55,72} As tabulated in Table 1, the nonradiative recombination times (τ) for both $(\text{BA})_2\text{PbBr}_4$ and $(\text{PEA})_2\text{PbBr}_4$ are estimated to be on the nanosecond scale. Moreover, the nonradiative recombination time for $(\text{PEA})_2\text{PbBr}_4$ is about 3 times larger than that for $(\text{BA})_2\text{PbBr}_4$. The longer carrier lifetime of $(\text{PEA})_2\text{PbBr}_4$ compared to $(\text{BA})_2\text{PbBr}_4$ agrees well with the experimental photoluminescence reported recently.¹¹ Thus, our simulations imply the dominant influences of spacer cations on the excited-state carrier dynamics in 2D bromide perovskites.

To have an in-depth understanding of the excited-state quantum dynamics, we investigate coupling of electronic and lattice degrees of freedom. Previous studies find that both elastic and inelastic carrier scattering, induced by electron–phonon coupling, play an important role in determining the nonradiative carrier recombination time.^{55,72,75,76} First, we focus on the inelastic electron–phonon scattering that underpins the exchange of energy between electronic and vibrational subsystems. The nonradiative carrier recombination leads to an excess of electronic energy, the inelastic scattering process transfers this extra energy to nuclear degrees of freedom.⁷⁷ The nonadiabatic coupling (NAC) strength quantifies the extent of the inelastic scattering and consequently influences the recombination processes in these materials.^{78–80} Generally, the stronger the NAC, the faster the nonradiative carrier recombination occurs. Considering the

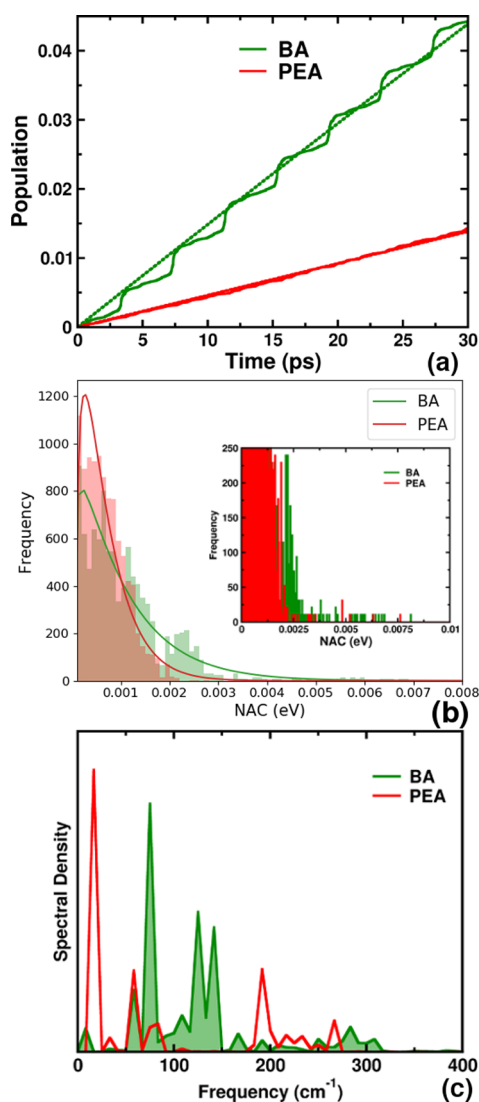


Figure 5. Effect of spacer cations on nonradiative carrier recombination and nonadiabatic coupling (NAC). (a) Population of recombined electron–hole in $(\text{BA})_2\text{PbBr}_4$ and $(\text{PEA})_2\text{PbBr}_4$ over time. The dashed lines are a fitted function with the population data, $f(t) = 1 - \exp(-t/\tau)$, τ is the carrier recombination time. (b) Histogram of absolute NAC values with magnitude >0.0001 eV. Plotted NAC has been calculated between VBM and CBM for 2D perovskites. BA-based perovskites exhibit more number of high NAC over simulation time. The inset shows the histogram of the full range of NAC values. (c) Fourier transform of autocorrelation for the band gap fluctuations of BA- and PEA-based 2D perovskites. The band gaps along the AIMD trajectories were calculated using DFT-based simulations as implemented in Vienna Ab Initio Simulation Package (VASP) and using eq 2 in the Supporting Information to calculate the autocorrelation. Involved frequencies with broader ranges for BA-based perovskite indicate their stronger NAC relative to the PEA-based one.

fact that intraband relaxations typically appear on the femtosecond time scale (see Figure S2 and section S3 in the Supporting Information), we reasonably approximate that all excited carriers, i.e., electrons and holes, relax to band edges prior to the recombining across the band gap in these 2D perovskites.^{27,74,81} Thus, we particularly focus on the NAC between the VBM and CBM states. Canonically averaged absolute values as tabulated in Table 1 show only slightly

Table 1. HSE06+SOC Calculated Band Gaps, Nonradiative Carrier Recombination Times, Average Absolute Values of NACs, and Homogeneous (HLW) and Inhomogeneous (ILW) Line Widths in $(\text{BA})_2\text{PbBr}_4$ and $(\text{PEA})_2\text{PbBr}_4$

perovskites	band gap (eV)	recombination (ps)	NAC (eV)	HLW/ILW (meV)
$(\text{BA})_2\text{PbBr}_4$	3.13	668	0.014	155/172
$(\text{PEA})_2\text{PbBr}_4$	3.14	2158	0.012	123/133

stronger NAC for $(\text{BA})_2\text{PbBr}_4$ compared to that for $(\text{PEA})_2\text{PbBr}_4$. Furthermore, we analyze the instantaneous NAC values along the complete AIMD trajectory to find their fluctuations over time at simulation conditions. Plotted histogram in Figure 5b exhibits more occurrences of high NAC values (>0.0001) for $(\text{BA})_2\text{PbBr}_4$ than for $(\text{PEA})_2\text{PbBr}_4$. As only high instantaneous NAC values are relevant for determining the nonradiative carrier recombination rates, we particularly focus on such occurrences. Each large instantaneous NAC value indicates high probability for nonradiative electron–hole recombination. This explains faster carrier recombination in the $(\text{BA})_2\text{PbBr}_4$, as found in Figure 5a. At the atomistic level, stronger wave function mixing of the participating states, i.e., CBM and VBM, leads to higher NAC values. Wave function mixing further depends on the nuclear dynamics of the atoms contributing to band edge states. More nuclear fluctuations of these atoms promote larger wave function mixing between the VBM and VBM, resulting in stronger NAC. Here, the PbBr_4 framework where the VBM and CBM (see Figure 3) wave functions remain delocalized, exhibits more flexibility for $(\text{BA})_2\text{PbBr}_4$ (see Figure 2). This consequently results in the occurrence of higher instantaneous NAC values for this BA-based 2D perovskite compared to the PEA-based one.

The very dissimilar nonradiative recombination dynamics in 2D bromide perovskites originates from their spacer-cation dependent structural dynamics, which in turn results in different inelastic electron–phonon scattering. Our results are in agreement with the recent resonance Raman (RR) spectroscopy-based experiments, which also indicates higher electron–phonon coupling for $(\text{BA})_2\text{PbBr}_4$ compared to PEA-based perovskite.¹¹

The significant role of spacer cation– PbBr_4 dynamics on the excited-state carrier recombination demands in-depth understanding of electron–phonon interactions in these 2D perovskites. To this end, we calculate the phonon modes that couple to the electronic subsystem and participate in electron–phonon scattering processes at room temperature. The Fourier transformation (FT) of the autocorrelation function (ACF) of the band gaps, identifies these active phonon modes (see the Supporting Information section S4 for details). Spectral densities plotted in Figure 5c show all the peaks to appear below 400 cm^{-1} . Thus, only the low-frequency phonon modes participate in the nonradiative relaxation of photoexcited carriers across the band-gaps in these 2D perovskites as found for other similar materials.^{73,75,76,82} It is worth mentioning that due to the presence of C–H and N–H bonds in spacer cations, the vibrational spectra have modes appearing at high frequency ranges, $>3200\text{ cm}^{-1}$.⁸³ However, as the charge densities of the band edge states remain delocalized only on the inorganic PbBr_4 sublattice, these cationic high-frequency phonon modes do not contribute directly to the carrier recombination process. Focusing on the

low-frequency range, we find phonon modes appearing below 100 cm^{-1} attribute to different Pb–Br bending and stretching motions.⁸⁴ As both $(\text{BA})_2\text{PbBr}_4$ and $(\text{PEA})_2\text{PbBr}_4$ have comparable PbBr frames, the Pb–Br peaks mostly superimpose in this range of frequency. However, phonon modes in the frequency range of $100\text{--}200\text{ cm}^{-1}$ differ significantly for two materials. These modes contribute to coupled dynamics between the spacer cations and PbBr_4 sublattice.^{85,86} The number of higher frequency peaks (in the range $>100\text{ cm}^{-1}$ and $<200\text{ cm}^{-1}$) for the $(\text{BA})_2\text{PbBr}_4$ perovskite demonstrates the presence of phonon modes that actively participate in electron–phonon coupling.^{55,86–88} Participation of higher frequency phonons during electron–hole recombinations in $(\text{BA})_2\text{PbBr}_4$, further justifies their larger NAC compared to that in $(\text{PEA})_2\text{PbBr}_4$ perovskite. Thus, the more flexible structure of $(\text{BA})_2\text{PbBr}_4$ strengthens the instantaneous NAC interactions. Note that vibrational modes with frequency $>200\text{ cm}^{-1}$ play a minor role in electron–phonon interactions, as such high frequencies arise due to the predominately molecular motions.^{11,86,88}

When considering elastic electron–phonon scattering, the nonradiative charge recombination produces superpositions between pairs of participating-state wave functions (i.e., VBM and CBM) as a result of the NAC.⁷⁷ The elastic scattering induces quantum decoherence and hinders this superposition between the participating states. The decoherence further suppresses the quantum transition representing the charge recombination and consequently enhances the photogenerated carrier lifetime as the demonstration of the Turing paradox. However, as detailed in section S3 of the Supporting Information, we find that rates of decoherence for $(\text{BA})_2\text{PbBr}_4$ and $(\text{PEA})_2\text{PbBr}_4$ are very similar and consequently the elastic scattering is not a key component in justifying their very different charge carrier recombination time.

Among several factors, the carrier recombination rate mostly depends on the band gap, dephasing time, and NAC strength.⁸⁹ The rate changes inversely with the band gap whereas it varies proportionally with the square of the nonadiabatic coupling strength as described in Fermi's Golden rule.^{89,90} Moreover, according to Franck–Condon principle, a short dephasing time reduces the electronic transition probability amplitude and consequently increases the carrier recombination time.^{91,92} As the band gap and dephasing time are similar for $(\text{BA})_2\text{PbBr}_4$ and $(\text{PEA})_2\text{PbBr}_4$ (see section S3 in the Supporting Information), the significant difference in their carrier recombination dynamics originates from the NAC strength. The stronger instantaneous as well as time-averaged NAC in $(\text{BA})_2\text{PbBr}_4$ dominantly determines their much faster nonradiative carrier recombination rate compared to that of PEA-based perovskite.

Along with the nonradiative recombination rates, these simulations also provide an estimate for PL line width, which is an important parameter for the purity of the emitted light in an LED device.^{34,37} The inhomogeneous line-broadening originates from the phonon-induced electronic energy gap fluctuations and can be calculated as the square root of the unnormalized autocorrelation functions at initial time, $C_{ij}(0)$. From $C_{ij}(0)$ values as plotted in the inset of Figure S4, we find the inhomogeneous line-broadening for $(\text{BA})_2\text{PbBr}_4$ and $(\text{PEA})_2\text{PbBr}_4$ perovskites are 172 and 133 meV, respectively. The other contribution to the line broadening that is the homogeneous line width can be formulated as the reduced Planck's constant times the inverse of pure-dephasing time (τ),

\hbar/τ .⁹³ Similar to inhomogeneous line broadening, as tabulated in Table 1, we find wider homogeneous broadening of $(\text{BA})_2\text{PbBr}_4$ compared to $(\text{PEA})_2\text{PbBr}_4$ perovskites. Thus, both the contributions indicate a broadened band edge PL peak for $(\text{BA})_2\text{PbBr}_4$ relative to that for $(\text{PEA})_2\text{PbBr}_4$, implying narrower emission from the later. The present trend of the line widths agrees very well with the room-temperature photoluminescence spectra reported by Gong et al.¹¹ Thus, rigidity in 2D perovskites not only suppresses the nonradiative carrier relaxation but also enhances the color-purity of emitted light.

In conclusion, we explore room temperature structural fluctuations for monolayer lead bromide 2D perovskites, containing very different spacer cations. We find that long-alkyl-chain-based cations result in more fluctuating structure at ambient conditions compared to the phenyl-group-based one. Time-domain *ab initio* simulations demonstrate that the nonradiative recombination rate for more fluctuating $(\text{BA})_2\text{PbBr}_4$ is much higher than the rate for comparatively rigid $(\text{PEA})_2\text{PbBr}_4$. Stronger nonadiabatic coupling between band-edge states of the more flexible $(\text{BA})_2\text{PbBr}_4$ causes the higher probability of nonradiative electron–hole recombination compared to the other material. The latter substantially reduces the luminescence quantum yield for $(\text{BA})_2\text{PbBr}_4$ compared to that for $(\text{PEA})_2\text{PbBr}_4$. This further reveals an influence of spacer cations on the excited-state carrier dynamics in 2D perovskites. The much narrower PL line width of $(\text{PEA})_2\text{PbBr}_4$ also indicates their color pure emission characteristics, highly desirable for solid-state lighting devices.

Overall, our work links electron–lattice dynamics and emission properties of recently emerged 2D halide perovskites. Despite the absence of direct involvement of spacer cations to the band edge states of these materials, their structural packing and dynamical coupling to the PbBr-framework is expected to play a decisive role in LED performance. Thus, selection of appropriate spacer cations becomes an important design principle for realizing high performing 2D halide perovskite-based light-emitting devices. The spacer cations need to be less flexible and their dynamics should weakly couple to the metal halide framework. An aromatic ring containing spacers with strong interlayer $\pi\text{--}\pi$, $\text{XH}\text{--}\pi$ (X = electronegative elements) stacking, and the introduction of dicationic molecules as a spacer are a couple of promising approaches to enhance the rigidity of these 2D perovskites.⁹⁴ Compositional engineering by incorporating different sized cations inside the inorganic framework of multilayered perovskites can further increase the mechanical strength and consequently result in reduced cation-framework coupling.⁶ Based on the fundamental understanding of the structure-excited-state properties, our present work represents the molecular engineering as a promising route to widely tune the light-emitting properties of emerging 2D metal halide perovskites.

Computational Methods. For static density functional theory (DFT) calculations and *ab initio* molecular dynamics (AIMD) simulations, we have used VASP.^{95,96} We applied the projected augmented wave (PAW) method within a plane-wave basis set of cutoff energy of 520 eV for all static calculations.⁹⁷ The generalized gradient approximation (GGA) with the Perdew–Burke–Ernzerhof functional (PBE) form has been used to capture the exchange and correlation interactions.⁹⁸ All interatomic forces of simulation cells, containing four formula units of $(\text{BA})_2\text{PbBr}_4$ (156 atoms) and $(\text{PEA})_2\text{PbBr}_4$ (188 atoms), were relaxed to less than $0.01\text{ eV}\text{\AA}^{-1}$ during geometry

optimization. The DFT-D3 method as formulated by Grimme⁹⁹ and a $4 \times 4 \times 1$ Γ -centered Monkhorst–Pack¹⁰⁰ mesh were considered for both 2D perovskites. To calculate more accurate electronic structures, spin–orbit coupling (SOC) and the screened hybrid functionals of Heyd–Scuseria–Ernzerhof (HSE06) were further applied self-consistently.¹⁰¹ We set the Hartree–Fock exchange to 43% and the empirical range-separation parameter $\omega = 0.11$ bohr⁻¹ for the HSE06 functionals. These computational parameters have been widely used to model the near band-edge electronic structure of hybrid halide perovskites.⁶⁶

To investigate the charge carrier dynamics, the mixed quantum-classical NAMD simulations were considered by applying the decoherence-induced surface hopping (DISH) technique.^{102,103} According to this approach the electrons and nuclei are considered as quantum mechanical and semiclassical entities, respectively. The excited-state dynamics of inorganic and hybrid perovskites have been extensively studied by this method recently.^{55,78,79,82} For AIMD simulations we considered a $2 \times 2 \times 1$ Monkhorst–Pack k-point mesh, plane-wave energy cutoff of 400 eV and time step of 1 fs. For these AIMD calculations we used PBE-GGA exchange–correlation functions and DFT-D3 corrections. We started with the 0 K DFT optimized structures and heated these to 300 K using repeated velocity rescaling for 4 ps. Another 3 ps trajectories using the canonical ensemble were generated to ensure thermal equilibrium. Following that, we generate 4 ps trajectories in the microcanonical ensemble and used these for the non-adiabatic coupling simulations. We considered all 4000 geometries along the trajectories and 1000 stochastic realizations of the DISH process for each geometry to evaluate the electron–hole recombination as implemented in the PYthon eXtension for Ab Initio Dynamics code.^{104,105} We further calculate the pure-dephasing time as considered in the optical-response theory for evaluating the decoherence time for these materials.¹⁰⁶ Even though recent work points out the importance of SOC in nonradiative charge recombination, we have not included such an effect in our simulations due to very high computational cost.¹⁰⁷ Furthermore, the CBM and the VBM wave functions, which are dominantly involved in the electron–hole recombination process, are spatially located over the PbBr-frame for both 2D perovskites considered here (see Figure 3c–f). As the same heavy-atoms contribute to the band edges, we assume that the SOC will affect the recombination in these perovskites to a similar extent. It is also well established that SOC has a minor effect on the molecular dynamics trajectories.¹⁰⁸ Thus, we expect that the main conclusions of current NAMD simulations without considering the SOC effect will remain unaltered even after including the SOC corrections. Another strong approximation is exclusion of excitonic effects present in 2D perovskites. However, proper description of these effects requires time-dependent Bethe–Salpeter theory for dynamic lattices, a method that is not completely developed yet. More computational details have been included in section S4 in the Supporting Information.

■ ASSOCIATED CONTENT

SI Supporting Information

The Supporting Information is available free of charge at <https://pubs.acs.org/doi/10.1021/acs.jpcllett.0c00594>.

Details of (BA)₂PbBr₄ and (PEA)₂PbBr₄ structures and states, calculating the electron-hole recombination time, elastic electron–phonon interactions, autocorrelation function of band gap fluctuations over AIMD trajectories (PDF)

■ AUTHOR INFORMATION

Corresponding Authors

Dibyajyoti Ghosh – Theoretical Division and Center for Nonlinear Studies, Los Alamos National Laboratory, Los Alamos, New Mexico 87545, United States; orcid.org/0000-0002-3640-7537; Email: dibyajyoti@lanl.gov

Sergei Tretiak – Theoretical Division, Center for Nonlinear Studies, and Center for Integrated Nanotechnologies, Los Alamos National Laboratory, Los Alamos, New Mexico 87545, United States; orcid.org/0000-0001-5547-3647; Email: serg@lanl.gov

Author

Amand J. Neukirch – Theoretical Division, Los Alamos National Laboratory, Los Alamos, New Mexico 87545, United States; orcid.org/0000-0002-6583-0086

Complete contact information is available at: <https://pubs.acs.org/doi/10.1021/acs.jpcllett.0c00594>

Notes

The authors declare no competing financial interest.

■ ACKNOWLEDGMENTS

The work at Los Alamos National Laboratory (LANL) was supported by the LANL LDRD program. This work was done in part at the Center for Nonlinear Studies (CNLS) and the Center for Integrated Nanotechnologies (CINT), a U.S. Department of Energy and Office of Basic Energy Sciences user facility, at LANL. This research used resources provided by the LANL Institutional Computing Program. Los Alamos National Laboratory is operated by Triad National Security, LLC, for the National Nuclear Security Administration of the U.S. Department of Energy (Contract No. 89233218NCA000001).

■ REFERENCES

- (1) Yuan, M.; Quan, L. N.; Comin, R.; Walters, G.; Sabatini, R.; Voznyy, O.; Hoogland, S.; Zhao, Y.; Beauregard, E. M.; Kanjanaboos, P. Perovskite energy funnels for efficient light-emitting diodes. *Nat. Nanotechnol.* **2016**, *11*, 872.
- (2) Smith, M. D.; Connor, B. A.; Karunadasa, H. I. Tuning the luminescence of layered halide perovskites. *Chem. Rev.* **2019**, *119*, 3104–3139.
- (3) Quan, L. N.; Zhao, Y.; García de Arquer, F. P.; Sabatini, R.; Walters, G.; Voznyy, O.; Comin, R.; Li, Y.; Fan, J. Z.; Tan, H. Tailoring the energy landscape in quasi-2D halide perovskites enables efficient green-light emission. *Nano Lett.* **2017**, *17*, 3701–3709.
- (4) Byun, J.; Cho, H.; Wolf, C.; Jang, M.; Sadhanala, A.; Friend, R. H.; Yang, H.; Lee, T.-W. Efficient Visible Quasi-2D Perovskite Light-Emitting Diodes. *Adv. Mater.* **2016**, *28*, 7515–7520.
- (5) Liang, D.; Peng, Y.; Fu, Y.; Shearer, M. J.; Zhang, J.; Zhai, J.; Zhang, Y.; Hamers, R. J.; Andrew, T. L.; Jin, S. Color-pure violet-light-emitting diodes based on layered lead halide perovskite nanoplates. *ACS Nano* **2016**, *10*, 6897–6904.
- (6) Liu, Y.; Cui, J.; Du, K.; Tian, H.; He, Z.; Zhou, Q.; Yang, Z.; Deng, Y.; Chen, D.; Zuo, X. Efficient blue light-emitting diodes based on quantum-confined bromide perovskite nanostructures. *Nat. Photonics* **2019**, *13*, 760–764.

- (7) Dohner, E. R.; Hoke, E. T.; Karunadasa, H. I. Self-assembly of broadband white-light emitters. *J. Am. Chem. Soc.* **2014**, *136*, 1718–1721.
- (8) Dohner, E. R.; Jaffe, A.; Bradshaw, L. R.; Karunadasa, H. I. Intrinsic white-light emission from layered hybrid perovskites. *J. Am. Chem. Soc.* **2014**, *136*, 13154–13157.
- (9) Biswas, A.; Bakthavatsalam, R.; Kundu, J. Efficient exciton to dopant energy transfer in Mn²⁺-doped (C₄H₉NH₃)₂PbBr₄ two-dimensional (2D) layered perovskites. *Chem. Mater.* **2017**, *29*, 7816–7825.
- (10) Mao, L.; Wu, Y.; Stoumpos, C. C.; Wasielewski, M. R.; Kanatzidis, M. G. White-light emission and structural distortion in new corrugated two-dimensional lead bromide perovskites. *J. Am. Chem. Soc.* **2017**, *139*, 5210–5215.
- (11) Gong, X.; Voznyy, O.; Jain, A.; Liu, W.; Sabatini, R.; Piontkowski, Z.; Walters, G.; Bappi, G.; Nokhrin, S.; Bushuyev, O. Electron–phonon interaction in efficient perovskite blue emitters. *Nat. Mater.* **2018**, *17*, 550.
- (12) Tsai, H.; Nie, W.; Blancon, J.-C.; Stoumpos, C. C.; Asadpour, R.; Harutyunyan, B.; Neukirch, A. J.; Verduzco, R.; Crochet, J. J.; Tretiak, S. High-efficiency two-dimensional Ruddlesden–Popper perovskite solar cells. *Nature* **2016**, *536*, 312.
- (13) Pedesseau, L.; Saponi, D.; Traore, B.; Robles, R.; Fang, H.-H.; Loi, M. A.; Tsai, H.; Nie, W.; Blancon, J.-C.; Neukirch, A. Advances and promises of layered halide hybrid perovskite semiconductors. *ACS Nano* **2016**, *10*, 9776–9786.
- (14) Smith, M. D.; Jaffe, A.; Dohner, E. R.; Lindenberg, A. M.; Karunadasa, H. I. Structural origins of broadband emission from layered Pb–Br hybrid perovskites. *Chem. Sci.* **2017**, *8*, 4497–4504.
- (15) Dou, L.; Wong, A. B.; Yu, Y.; Lai, M.; Kornienko, N.; Eaton, S. W.; Fu, A.; Bischak, C. G.; Ma, J.; Ding, T. Atomically thin two-dimensional organic–inorganic hybrid perovskites. *Science* **2015**, *349*, 1518–1521.
- (16) Mitzi, D. B. Synthesis, crystal structure, and optical and thermal properties of (C₄H₉NH₃)₂M₂I₄ (M = Ge, Sn, Pb). *Chem. Mater.* **1996**, *8*, 791–800.
- (17) Stoumpos, C. C.; Cao, D. H.; Clark, D. J.; Young, J.; Rondinelli, J. M.; Jang, J. I.; Hupp, J. T.; Kanatzidis, M. G. Ruddlesden–Popper hybrid lead iodide perovskite 2D homologous semiconductors. *Chem. Mater.* **2016**, *28*, 2852–2867.
- (18) Stoumpos, C. C.; Soe, C. M. M.; Tsai, H.; Nie, W.; Blancon, J.-C.; Cao, D. H.; Liu, F.; Traoré, B.; Katan, C.; Even, J. High members of the 2D Ruddlesden–Popper halide perovskites: synthesis, optical properties, and solar cells of (CH₃(CH₂)₃NH₃)₂(CH₃NH₃)₄Pb₂I₁₆. *Chem.* **2017**, *2*, 427–440.
- (19) Guo, Z.; Wu, X.; Zhu, T.; Zhu, X.; Huang, L. Electron-phonon scattering in atomically thin 2D perovskites. *ACS Nano* **2016**, *10*, 9992–9998.
- (20) Leveille, J.; Katan, C.; Even, J.; Ghosh, D.; Nie, W.; Mohite, A. D.; Tretiak, S.; Schleife, A.; Neukirch, A. J. Tuning electronic structure in layered hybrid perovskites with organic spacer substitution. *Nano Lett.* **2019**, *19*, 8732.
- (21) Blancon, J.-C.; Tsai, H.; Nie, W.; Stoumpos, C. C.; Pedesseau, L.; Katan, C.; Kepenekian, M.; Soe, C. M. M.; Appavoo, K.; Sfeir, M. Y. Extremely efficient internal exciton dissociation through edge states in layered 2D perovskites. *Science* **2017**, *355*, 1288–1292.
- (22) Katan, C.; Mercier, N.; Even, J. Quantum and dielectric confinement effects in lower-dimensional hybrid perovskite semiconductors. *Chem. Rev.* **2019**, *119*, 3140–3192.
- (23) Chen, Y.; Sun, Y.; Peng, J.; Zhang, W.; Su, X.; Zheng, K.; Pullerits, T.; Liang, Z. Tailoring Organic Cation of 2D Air-Stable Organometal Halide Perovskites for Highly Efficient Planar Solar Cells. *Adv. Energy Mater.* **2017**, *7*, 1700162.
- (24) Mao, L.; Stoumpos, C. C.; Kanatzidis, M. G. Two-dimensional hybrid halide perovskites: principles and promises. *J. Am. Chem. Soc.* **2019**, *141*, 1171–1190.
- (25) Zhang, F.; Kim, D. H.; Lu, H.; Park, J.-S.; Larson, B. W.; Hu, J.; Gao, L.; Xiao, C.; Reid, O. G.; Chen, X. Enhanced charge transport in 2D perovskites via fluorination of organic cation. *J. Am. Chem. Soc.* **2019**, *141*, 5972–5979.
- (26) Blancon, J.-C.; Stier, A. V.; Tsai, H.; Nie, W.; Stoumpos, C. C.; Traore, B.; Pedesseau, L.; Kepenekian, M.; Katsutani, F.; Noe, G. Scaling law for excitons in 2D perovskite quantum wells. *Nat. Commun.* **2018**, *9*, 2254.
- (27) Zhang, S.-F.; Chen, X.-K.; Ren, A.-M.; Li, H.; Bredas, J.-L. Impact of Organic Spacers on the Carrier Dynamics in 2D Hybrid Lead-Halide Perovskites. *ACS Energy Lett.* **2019**, *4*, 17–25.
- (28) Yang, X.; Xu, X.; Zhou, G. Recent advances of the emitters for high performance deep-blue organic light-emitting diodes. *J. Mater. Chem. C* **2015**, *3*, 913–944.
- (29) Wu, Z.; Ji, C.; Sun, Z.; Wang, S.; Zhao, S.; Zhang, W.; Li, L.; Luo, J. Broadband white-light emission with a high color rendering index in a two-dimensional organic–inorganic hybrid perovskite. *J. Mater. Chem. C* **2018**, *6*, 1171–1175.
- (30) Nanishi, Y. Nobel Prize in Physics: The birth of the blue LED. *Nat. Photonics* **2014**, *8*, 884.
- (31) Kondo, Y.; Yoshiura, K.; Kitera, S.; Nishi, H.; Oda, S.; Gotoh, H.; Sasada, Y.; Yanai, M.; Hatakeyama, T. Narrowband deep-blue organic light-emitting diode featuring an organoboron-based emitter. *Nat. Photonics* **2019**, *13*, 678–682.
- (32) Tsukazaki, A.; Kubota, M.; Ohtomo, A.; Onuma, T.; Ohtani, K.; Ohno, H.; Chichibu, S. F.; Kawasaki, M. Blue light-emitting diode based on ZnO. *Jpn. J. Appl. Phys.* **2005**, *44*, L643.
- (33) Shirasaki, Y.; Supran, G. J.; Bawendi, M. G.; Bulović, V. Emergence of colloidal quantum-dot light-emitting technologies. *Nat. Photonics* **2013**, *7*, 13.
- (34) Stranks, S. D.; Snaith, H. J. Metal-halide perovskites for photovoltaic and light-emitting devices. *Nat. Nanotechnol.* **2015**, *10*, 391.
- (35) Comin, R.; Walters, G.; Thibau, E. S.; Voznyy, O.; Lu, Z.-H.; Sargent, E. H. Structural, optical, and electronic studies of wide-bandgap lead halide perovskites. *J. Mater. Chem. C* **2015**, *3*, 8839–8843.
- (36) Li, G.; Rivarola, F. W. R.; Davis, N. J.; Bai, S.; Jellicoe, T. C.; de la Peña, F.; Hou, S.; Ducati, C.; Gao, F.; Friend, R. H. Highly efficient perovskite nanocrystal light-emitting diodes enabled by a universal crosslinking method. *Adv. Mater.* **2016**, *28*, 3528–3534.
- (37) Yao, E.-P.; Yang, Z.; Meng, L.; Sun, P.; Dong, S.; Yang, Y.; Yang, Y. High-Brightness Blue and White LEDs based on Inorganic Perovskite Nanocrystals and their Composites. *Adv. Mater.* **2017**, *29*, 1606859.
- (38) Gangishetty, M. K.; Hou, S.; Quan, Q.; Congreve, D. N. Reducing Architecture Limitations for Efficient Blue Perovskite Light-Emitting Diodes. *Adv. Mater.* **2018**, *30*, 1706226.
- (39) Vashishtha, P.; Halpert, J. E. Field-driven ion migration and color instability in red-emitting mixed halide perovskite nanocrystal light-emitting diodes. *Chem. Mater.* **2017**, *29*, 5965–5973.
- (40) Huang, H.; Polavarapu, L.; Sichert, J. A.; Susa, A. S.; Urban, A. S.; Rogach, A. L. Colloidal lead halide perovskite nanocrystals: synthesis, optical properties and applications. *NPG Asia Mater.* **2016**, *8*, No. e328.
- (41) Kim, Y.-H.; Wolf, C.; Kim, Y.-T.; Cho, H.; Kwon, W.; Do, S.; Sadhanala, A.; Park, C. G.; Rhee, S.-W.; Im, S. H. Highly efficient light-emitting diodes of colloidal metal–halide perovskite nanocrystals beyond quantum size. *ACS Nano* **2017**, *11*, 6586–6593.
- (42) Wood, V.; Panzer, M. J.; Caruge, J.-M.; Halpert, J. E.; Bawendi, M. G.; Bulovic, V. Air-stable operation of transparent, colloidal quantum dot based LEDs with a unipolar device architecture. *Nano Lett.* **2010**, *10*, 24–29.
- (43) Zhitomirsky, D.; Voznyy, O.; Hoogland, S.; Sargent, E. H. Measuring charge carrier diffusion in coupled colloidal quantum dot solids. *ACS Nano* **2013**, *7*, 5282–5290.
- (44) Seth, S.; Mondal, N.; Patra, S.; Samanta, A. Fluorescence blinking and photoactivation of all-inorganic perovskite nanocrystals CsPbBr₃ and CsPbBr₂I. *J. Phys. Chem. Lett.* **2016**, *7*, 266–271.
- (45) Congreve, D. N.; Weidman, M. C.; Seitz, M.; Paritmongkol, W.; Dahod, N. S.; Tisdale, W. A. Tunable light-emitting diodes

utilizing quantum-confined layered perovskite emitters. *ACS Photonics* **2017**, *4*, 476–481.

(46) Chen, Z.; Zhang, C.; Jiang, X.-F.; Liu, M.; Xia, R.; Shi, T.; Chen, D.; Xue, Q.; Zhao, Y.-J.; Su, S. High-performance color-tunable perovskite light emitting devices through structural modulation from bulk to layered film. *Adv. Mater.* **2017**, *29*, 1603157.

(47) Wang, Z.; McMeekin, D. P.; Sakai, N.; van Reenen, S.; Wojciechowski, K.; Patel, J. B.; Johnston, M. B.; Snaith, H. J. Efficient and Air-Stable Mixed-Cation Lead Mixed-Halide Perovskite Solar Cells with n-Doped Organic Electron Extraction Layers. *Adv. Mater.* **2017**, *29*, 1604186.

(48) Kumar, S.; Jagielski, J.; Kallikounis, N.; Kim, Y.-H.; Wolf, C.; Jenny, F.; Tian, T.; Hofer, C. J.; Chiu, Y.-C.; Stark, W. J. Ultrapure green light-emitting diodes using two-dimensional formamidinium perovskites: Achieving recommendation 2020 color coordinates. *Nano Lett.* **2017**, *17*, 5277–5284.

(49) Milot, R. L.; Sutton, R. J.; Eperon, G. E.; Haghighirad, A. A.; Martinez Hardigree, J.; Miranda, L.; Snaith, H. J.; Johnston, M. B.; Herz, L. M. Charge-carrier dynamics in 2D hybrid metal–halide perovskites. *Nano Lett.* **2016**, *16*, 7001–7007.

(50) Saparov, B.; Mitzi, D. B. Organic–inorganic perovskites: structural versatility for functional materials design. *Chem. Rev.* **2016**, *116*, 4558–4596.

(51) Kawano, N.; Koshimizu, M.; Sun, Y.; Yahaba, N.; Fujimoto, Y.; Yanagida, T.; Asai, K. Effects of organic moieties on luminescence properties of organic–inorganic layered perovskite-type compounds. *J. Phys. Chem. C* **2014**, *118*, 9101–9106.

(52) Mitzi, D. B.; Dimitrakopoulos, C. D.; Kosbar, L. L. Structurally tailored organic–inorganic perovskites: optical properties and solution-processed channel materials for thin-film transistors. *Chem. Mater.* **2001**, *13*, 3728–3740.

(53) Xu, Z.; Mitzi, D. B.; Dimitrakopoulos, C. D.; Maxcy, K. R. Semiconducting perovskites (2-XC6H4C2H4NH3)2SnI4 (X = F, Cl, Br): steric interaction between the organic and inorganic layers. *Inorg. Chem.* **2003**, *42*, 2031–2039.

(54) Knutson, J. L.; Martin, J. D.; Mitzi, D. B. Tuning the band gap in hybrid tin iodide perovskite semiconductors using structural templating. *Inorg. Chem.* **2005**, *44*, 4699–4705.

(55) Zhang, Z.; Fang, W.-H.; Tokina, M. V.; Long, R.; Prezhdo, O. V. Rapid decoherence suppresses charge recombination in multi-layer 2D halide perovskites: Time-domain ab initio analysis. *Nano Lett.* **2018**, *18*, 2459–2466.

(56) Abdel-Baki, K.; Boitier, F.; Diab, H.; Lanty, G.; Jemli, K.; Lédée, F.; Garrot, D.; Deleporte, E.; Lauret, J. Exciton dynamics and non-linearities in two-dimensional hybrid organic perovskites. *J. Appl. Phys.* **2016**, *119*, 064301.

(57) Ghosh, D.; Walsh Atkins, P.; Islam, M. S.; Walker, A. B.; Eames, C. Good Vibrations: Locking of Octahedral Tilting in Mixed-Cation Iodide Perovskites for Solar Cells. *ACS Energy Lett.* **2017**, *2*, 2424–2429.

(58) Ghosh, D.; Smith, A. R.; Walker, A. B.; Islam, M. S. Mixed A-Cation Perovskites for Solar Cells: Atomic-Scale Insights Into Structural Distortion, Hydrogen Bonding, and Electronic Properties. *Chem. Mater.* **2018**, *30*, 5194–5204.

(59) Ghosh, D.; Acharya, D.; Zhou, L.; Nie, W.; Prezhdo, O. V.; Tretiak, S.; Neukirch, A. J. Lattice Expansion in Hybrid Perovskites: Effect on Optoelectronic Properties and Charge Carrier Dynamics. *J. Phys. Chem. Lett.* **2019**, *10*, 5000–5007.

(60) Mayers, M. Z.; Tan, L. Z.; Egger, D. A.; Rappe, A. M.; Reichman, D. R. How lattice and charge fluctuations control carrier dynamics in halide perovskites. *Nano Lett.* **2018**, *18*, 8041–8046.

(61) Munson, K. T.; Swartzfager, J. R.; Asbury, J. B. Lattice Anharmonicity: A Double-Edged Sword for 3D Perovskite-Based Optoelectronics. *ACS Energy Lett.* **2019**, *4*, 1888–1897.

(62) Hedley, G. J.; Quarti, C.; Harwell, J.; Prezhdo, O. V.; Beljonne, D.; Samuel, I. D. Hot-hole cooling controls the initial ultrafast relaxation in methylammonium lead iodide perovskite. *Sci. Rep.* **2018**, *8*, 8115.

(63) Even, J.; Pedesseau, L.; Jancu, J.-M.; Katan, C. DFT and $k \cdot p$ modelling of the phase transitions of lead and tin halide perovskites for photovoltaic cells. *Phys. Status Solidi RRL* **2014**, *8*, 31–35.

(64) Even, J.; Pedesseau, L.; Jancu, J.-M.; Katan, C. Importance of spin–orbit coupling in hybrid organic/inorganic perovskites for photovoltaic applications. *J. Phys. Chem. Lett.* **2013**, *4*, 2999–3005.

(65) Yin, J.; Maity, P.; Xu, L.; El-Zohry, A. M.; Li, H.; Bakr, O. M.; Brédas, J.-L.; Mohammed, O. F. Layer-dependent Rashba band splitting in 2D hybrid perovskites. *Chem. Mater.* **2018**, *30*, 8538–8545.

(66) Meggiolaro, D.; De Angelis, F. First-Principles Modeling of Defects in Lead Halide Perovskites: Best Practices and Open Issues. *ACS Energy Lett.* **2018**, *3*, 2206–2222.

(67) Stroppa, A.; Di Sante, D.; Barone, P.; Bokdam, M.; Kresse, G.; Franchini, C.; Whangbo, M.-H.; Picozzi, S. Tunable ferroelectric polarization and its interplay with spin–orbit coupling in tin iodide perovskites. *Nat. Commun.* **2014**, *5*, 5900.

(68) Yaffe, O.; Guo, Y.; Tan, L. Z.; Egger, D. A.; Hull, T.; Stoumpos, C. C.; Zheng, F.; Heinz, T. F.; Kronik, L. Local polar fluctuations in lead halide perovskite crystals. *Phys. Rev. Lett.* **2017**, *118*, 136001.

(69) Niesner, D.; Hauck, M.; Shrestha, S.; Levchuk, I.; Matt, G. J.; Osvet, A.; Batentschuk, M.; Brabec, C.; Weber, H. B.; Fauster, T. Structural fluctuations cause spin-split states in tetragonal (CH₃NH₃)PbI₃ as evidenced by the circular photogalvanic effect. *Proc. Natl. Acad. Sci. U. S. A.* **2018**, *115*, 9509–9514.

(70) Motta, C.; El-Mellouhi, F.; Kais, S.; Tabet, N.; Alharbi, F.; Sanvito, S. Revealing the role of organic cations in hybrid halide perovskite CH₃NH₃PbI₃. *Nat. Commun.* **2015**, *6*, 7026.

(71) Ma, J.; Wang, L.-W. Nanoscale charge localization induced by random orientations of organic molecules in hybrid perovskite CH₃NH₃PbI₃. *Nano Lett.* **2015**, *15*, 248–253.

(72) He, J.; Fang, W.-H.; Long, R.; Prezhdo, O. V. Increased Lattice Stiffness Suppresses Nonradiative Charge Recombination in MAPbI₃ Doped with Larger Cations: Time-Domain Ab Initio Analysis. *ACS Energy Lett.* **2018**, *3*, 2070–2076.

(73) Jankowska, J.; Long, R.; Prezhdo, O. V. Quantum dynamics of photogenerated charge carriers in hybrid perovskites: Dopants, grain boundaries, electric order, and other realistic aspects. *ACS Energy Lett.* **2017**, *2*, 1588–1597.

(74) Nijamudheen, A.; Akimov, A. V. Criticality of symmetry in rational design of chalcogenide perovskites. *J. Phys. Chem. Lett.* **2018**, *9*, 248–257.

(75) Li, W.; Tang, J.; Casanova, D.; Prezhdo, O. V. Time-domain ab initio analysis rationalizes the unusual temperature dependence of charge carrier relaxation in lead halide perovskite. *ACS Energy Lett.* **2018**, *3*, 2713–2720.

(76) Tong, C.-J.; Li, L.; Liu, L.-M.; Prezhdo, O. V. Long Carrier Lifetimes in PbI₂-Rich Perovskites Rationalized by Ab Initio Nonadiabatic Molecular Dynamics. *ACS Energy Lett.* **2018**, *3*, 1868–1874.

(77) Neukirch, A. J.; Hyeon-Deuk, K.; Prezhdo, O. V. Time-domain ab initio modeling of excitation dynamics in quantum dots. *Coord. Chem. Rev.* **2014**, *263*, 161–181.

(78) Long, R.; Liu, J.; Prezhdo, O. V. Unravelling the effects of grain boundary and chemical doping on electron–hole recombination in CH₃NH₃PbI₃ perovskite by time-domain atomistic simulation. *J. Am. Chem. Soc.* **2016**, *138*, 3884–3890.

(79) He, J.; Vasenko, A. S.; Long, R.; Prezhdo, O. V. Halide composition controls electron–hole recombination in cesium–lead halide perovskite quantum dots: a time domain ab initio study. *J. Phys. Chem. Lett.* **2018**, *9*, 1872–1879.

(80) Li, W.; Sun, Y.-Y.; Li, L.; Zhou, Z.; Tang, J.; Prezhdo, O. V. Control of charge recombination in perovskites by oxidation state of halide vacancy. *J. Am. Chem. Soc.* **2018**, *140*, 15753–15763.

(81) Habenicht, B. F.; Craig, C. F.; Prezhdo, O. V. Time-domain ab initio simulation of electron and hole relaxation dynamics in a single-wall semiconducting carbon nanotube. *Phys. Rev. Lett.* **2006**, *96*, 187401.

- (82) Li, W.; Liu, J.; Bai, F.-Q.; Zhang, H.-X.; Prezhdo, O. V. Hole trapping by iodine interstitial defects decreases free carrier losses in perovskite solar cells: a time-domain ab initio study. *ACS Energy Lett.* **2017**, *2*, 1270–1278.
- (83) Leguy, A. M.; Goñi, A. R.; Frost, J. M.; Skelton, J.; Brivio, F.; Rodríguez-Martínez, X.; Weber, O. J.; Pallipurath, A.; Alonso, M. L.; Campoy-Quiles, M. Dynamic disorder, phonon lifetimes, and the assignment of modes to the vibrational spectra of methylammonium lead halide perovskites. *Phys. Chem. Chem. Phys.* **2016**, *18*, 27051–27066.
- (84) Perez-Osorio, M. A.; Lin, Q.; Phillips, R. T.; Milot, R. L.; Herz, L. M.; Johnston, M. B.; Giustino, F. Raman spectrum of the organic–inorganic halide perovskite CH₃NH₃PbI₃ from first principles and high-resolution low-temperature Raman measurements. *J. Phys. Chem. C* **2018**, *122*, 21703–21717.
- (85) Pérez-Osorio, M. A.; Milot, R. L.; Filip, M. R.; Patel, J. B.; Herz, L. M.; Johnston, M. B.; Giustino, F. Vibrational properties of the organic–inorganic halide perovskite CH₃NH₃PbI₃ from theory and experiment: factor group analysis, first-principles calculations, and low-temperature infrared spectra. *J. Phys. Chem. C* **2015**, *119*, 25703–25718.
- (86) Dragomir, V. A.; Neutzner, S.; Quarti, C.; Cortecchia, D.; Petrozza, A.; Roorda, S.; Beljonne, D.; Leonelli, R.; Kandada, A. R. S.; Silva, C. Lattice vibrations and dynamic disorder in two-dimensional hybrid lead-halide perovskites. *arXiv:1812.05255* **2018**.
- (87) Straus, D. B.; Hurtado Parra, S.; Iotov, N.; Gebhardt, J.; Rappe, A. M.; Subotnik, J. E.; Kikkawa, J. M.; Kagan, C. R. Direct observation of electron–phonon coupling and slow vibrational relaxation in organic–inorganic hybrid perovskites. *J. Am. Chem. Soc.* **2016**, *138*, 13798–13801.
- (88) Zhang, Z.; Fang, W.-H.; Long, R.; Prezhdo, O. V. Exciton Dissociation and Suppressed Charge Recombination at 2D Perovskite Edges: Key Roles of Unsaturated Halide Bonds and Thermal Disorder. *J. Am. Chem. Soc.* **2019**, *141*, 15557–15566.
- (89) Long, R.; Prezhdo, O. V.; Fang, W. Nonadiabatic charge dynamics in novel solar cell materials. *Wiley Interdisciplinary Reviews: Computational Molecular Science* **2017**, *7*, No. e1305.
- (90) Englman, R.; Jortner, J. The energy gap law for non-radiative decay in large molecules. *J. Lumin.* **1970**, *1*, 134–142.
- (91) Prezhdo, O. V.; Rossky, P. J. Relationship between quantum decoherence times and solvation dynamics in condensed phase chemical systems. *Phys. Rev. Lett.* **1998**, *81*, 5294.
- (92) Prezhdo, O. V.; Rossky, P. J. Mean-field molecular dynamics with surface hopping. *J. Chem. Phys.* **1997**, *107*, 825–834.
- (93) Mukamel, S. *Principles of nonlinear optical spectroscopy*; Oxford university press: New York, 1995; Vol. 29.
- (94) Mao, L.; Ke, W.; Pedesseau, L.; Wu, Y.; Katan, C.; Even, J.; Wasielewski, M. R.; Stoumpos, C. C.; Kanatzidis, M. G. Hybrid Dion–Jacobson 2D lead iodide perovskites. *J. Am. Chem. Soc.* **2018**, *140*, 3775–3783.
- (95) Kresse, G.; Hafner, J. Ab initio molecular dynamics for liquid metals. *Phys. Rev. B: Condens. Matter Mater. Phys.* **1993**, *47*, 558.
- (96) Kresse, G.; Hafner, J. Ab initio molecular-dynamics simulation of the liquid-metal–amorphous-semiconductor transition in germanium. *Phys. Rev. B: Condens. Matter Mater. Phys.* **1994**, *49*, 14251.
- (97) Kresse, G.; Joubert, D. From ultrasoft pseudopotentials to the projector augmented-wave method. *Phys. Rev. B: Condens. Matter Mater. Phys.* **1999**, *59*, 1758.
- (98) Perdew, J. P.; Burke, K.; Ernzerhof, M. Generalized Gradient Approximation Made Simple. *Phys. Rev. Lett.* **1996**, *77*, 3865.
- (99) Grimme, S.; Antony, J.; Ehrlich, S.; Krieg, H. A consistent and accurate ab initio parametrization of density functional dispersion correction (DFT-D) for the 94 elements H–Pu. *J. Chem. Phys.* **2010**, *132*, 154104.
- (100) Monkhorst, H. J.; Pack, J. D. Special points for Brillouin-zone integrations. *Phys. Rev. B* **1976**, *13*, 5188.
- (101) Heyd, J.; Scuseria, G. E.; Ernzerhof, M. Hybrid functionals based on a screened Coulomb potential. *J. Chem. Phys.* **2003**, *118*, 8207–8215.
- (102) Jaeger, H. M.; Fischer, S.; Prezhdo, O. V. Decoherence-induced surface hopping. *J. Chem. Phys.* **2012**, *137*, 22A545.
- (103) Craig, C. F.; Duncan, W. R.; Prezhdo, O. V. Trajectory surface hopping in the time-dependent Kohn–Sham approach for electron–nuclear dynamics. *Phys. Rev. Lett.* **2005**, *95*, 163001.
- (104) Akimov, A. V.; Prezhdo, O. V. The PYXAID program for non-adiabatic molecular dynamics in condensed matter systems. *J. Chem. Theory Comput.* **2013**, *9*, 4959–4972.
- (105) Akimov, A. V.; Prezhdo, O. V. Advanced capabilities of the PYXAID program: integration schemes, decoherence effects, multi-excitonic states, and field–matter interaction. *J. Chem. Theory Comput.* **2014**, *10*, 789–804.
- (106) Hamm, P. *Principles of nonlinear optical spectroscopy: A practical approach*; University of Zurich, 2005; Vol. 41, p 77.
- (107) Li, W.; Zhou, L.; Prezhdo, O. V.; Akimov, A. V. Spin–orbit interactions greatly accelerate nonradiative dynamics in lead halide perovskites. *ACS Energy Lett.* **2018**, *3*, 2159–2166.
- (108) Amat, A.; Mosconi, E.; Ronca, E.; Quarti, C.; Umari, P.; Nazeeruddin, M. K.; Grätzel, M.; De Angelis, F. Cation-induced Band-gap Tuning in Organohalide Perovskites: Interplay of Spin–orbit Coupling and Octahedra Tilting. *Nano Lett.* **2014**, *14*, 3608–3616.